LAWRENCE
LIVERMORE
NATIONAL
LABORATORY

LLNL-PROC-564492

Wind prediction with multiple guide stars reduces tomographic errors and expands MOAO field of regard

S. M. Ammons, L. Poyneer, D. Gavel, R. Kupke, C. E. Max, L. Johnson

July 13, 2012

SPIE Astronomical Telescopes and Instrumentation
Amsterdam, Netherlands
July 1, 2012 through July 6, 2012

Disclaimer

Evidence that wind prediction with multiple guide stars reduces tomographic errors and expands MOAO field of regard

S. Mark Ammons*[a], Lisa Poyneer[a], Donald T. Gavel[b], Renate Kupke[b], Claire E. Max[b], Luke Johnson[c]

[a]Lawrence Fellow, Lawrence Livermore National Laboratory, Physics Division, L-210, 7000 East Ave., Livermore, CA USA 94550
[b]UCO/Lick Observatory, University of California, Santa Cruz, 1156 High St., Santa Cruz, CA USA 95064
[c]National Solar Observatory, 950 N. Cherry Ave., Tucson, AZ USA 85719

ABSTRACT

We explore the extension of predictive control techniques to multi-guide star, multi-layer tomographic wavefront measurement systems using a shift-and-average correction scheme that incorporates wind velocity and direction. In addition to reducing temporal error budget terms, there are potentially additional benefits for tomographic AO systems; the combination of wind velocity information and phase height information from multiple guide stars breaks inherent degeneracies in volumetric tomographic reconstruction, producing a reduction in the geometric tomographic error. In a tomographic simulation of an 8-meter telescope with 3 laser guide stars over 2 arcminute diameter, we find that tracking organized wind motion as it flows into metapupil regions sampled by only one guide star improves layer estimates beyond the guide star radius, allowing for an expansion of the field of view. For this case, we demonstrate improvement of layer phase estimates of 3% to 12%, translating into potential gains in the MOAO field of regard area of up to 40%. The majority of the benefits occur in regions of the metapupil sampled by only 1-2 LGS's downwind at high altitudes.

Keywords: adaptive optics, predictive control, laser guide star, tomography, MCAO, MOAO, LTAO, GLAO, LQG, Kalman

1. INTRODUCTION

A major disadvantage of the Sodium Laser Guide Star is the *cone effect,* or the insufficiency of a single laser guide star to probe a cylinder of turbulence leading to an object at essentially infinite altitude. As a result of this geometric mismatch, there are regions of turbulence outside of the sampled LGS cone that are unsensed. It is generally accepted that integrated wavefronts from multiple laser guide stars (LGS) contain the information needed to tomographically reconstruct the turbulent volume in the cylinder above the telescope, and thus the wavefront necessary to correct at any field position in the LGS constellation. This Laser Guide Star Tomographic Adaptive Optics (LTAO) solution has been rigorously envisioned and explored over the last decade.[1,2,3,4]

AO tomography is necessary for a number of instrument architectures that intend to achieve high precision correction on-axis (high-Strehl LTAO) or correction over wider fields of view (Multi-Conjugate or Multi-Object Adaptive Optics, MCAO/MOAO).[5,6,7] Unfortunately, tomographic wavefront estimation is subject to a number of errors, especially that due to the limited number of lines-of-sight available for integrating atmospheric wavefronts, which we refer to as the "geometric" tomographic error. This error is a function only of the geometry of the guide star constellation and the C_N^2 profile.

Geometric tomographic wavefront sensing error is an important error term for the next generation of multi-guide star AO systems planned for 8-10 meter telescopes and Extremely Large Telescopes (ELT). It is especially relevant for ELTs, for which the cone effect becomes a more dominant term, complicating efforts to improve AO correction precision. For

*ammons1@llnl.gov; phone 1 925 422-2102; www.u.arizona.edu/~ammons81/

laser tomographic AO systems, the geometric tomographic error is driven by the number of LGSs and their areal density, and thus closely tied to the expense of these systems. New techniques to reduce the tomographic error will be important for pushing LTAO to the visible wavelengths and MCAO/MOAO to wider fields.

In this paper, we present a simple shift-and-average scheme to predict wavefront phase in individual atmospheric layers if the wind vector is estimated by some other technique. We combine this method with a back-projection tomography solver[8] for a multi-layer atmosphere to show that the volumetric tomographic reconstruction can be improved under the assumption of 100% Taylor frozen flow turbulence. For the simulations we present in these proceedings, we do not consider measurement errors in the wavefront sensing, spatial frequencies beyond those sampled by the assumed wavefront sensor architecture, or wavefront sensor aliasing. Section 2 presents a short introduction to predictive wavefront control for multiple guide star systems. Section 3 describes the experimental setup of the simulation and section 4 concludes.

2. PREDICTIVE WAVEFRONT CONTROL UTILIZING TAYLOR FROZEN-FLOW MOTION

For turbulent evolution that can be described as pure Taylor frozen-flow motion, estimating wavefronts at future timesteps is easily done by shifting and interpolating previous wavefront measurements.[9,10,11,12] In principle, this sort of prediction averages over measurement noise, permitting the AO system to be run at a lower frame rate to achieve equivalent performance and enabling operation on fainter guide stars. The advantages of predictive wavefront control assuming Taylor frozen flow have been characterized[9,12] and frozen flow evolution has been observed at a variety of locations.[9,11] Other approaches include Linear Quadratic Gaussian (LQG) analysis, a type of predictive control that has been demonstrated in simulation and on testbeds.[13,7,14]

In multi-layer atmospheres, it is plausible that the tomographic error modes at each layer become decorrelated in time as the layers translate in different directions. In this case, shifting and averaging phase estimates from tomographic reconstructions in previous timesteps along the known wind vector could result in an improved estimate of each layer. Investigators of LQG control have shown that this technique, which takes advantage of known wind velocity, can reduce tomographic reconstruction error for integrated wavefronts in-between guide stars.[13]

Perhaps the most intriguing potential advantage to predictive tomography in the Taylor frozen flow regime is the widening of MOAO fields of view as wind is tracked beyond the metapupils sampled by guide stars. In regions of the metapupil sampled by only one guide star, no information about the height of measured phase is obtainable, so it is sensible that tracking phase into these regions can result in improved layer phase estimates at the edges of the guide star constellation. It is this hypothesis that we focus on for the simulations presented in Section 3.

Here, we present a simple example as an "existence proof" that tracking frozen flow motion in a three-dimensional atmosphere assists in tomographic reconstruction. We consider a simple 2-layer model in which the ground layer is static and the upper layer has some velocity v (left panel of Figure 1). The turbulent evolution is assumed to be 100% Taylor frozen flow. We assume that wavefront sensing is performed by LGSs, although the principle is extendable to natural guide stars as well. The geometry we have constructed is mathematically equivalent to a scenario with 2 static layers and mobile laser guide stars scanning in the reverse direction at an angular rate $\omega = v/h$, where h is the height of the layer (right panel of Figure 1). In this second situation, it is clear that the moving LGSs provide integrals of the wavefront through the volume at new sampling positions as time passes, and indeed may be tomographically analyzed simultaneously with LGS measurements at previous timesteps to densely sample the volume.

We use a back-projection tomographic simulator[8] to assess the performance of such a scenario. For an 8-meter telescope with 5 LGSs on a circle of 2' in a "quincunx" arrangement, we tomographically analyze LGS wavefronts from six previous timesteps simultaneously to densely sample the volume, effectively creating a "smeared" guide star constellation with 30 LGSs as shown in the subpanel of Figure 2. The tomographic error is on the order of ~30 nm for the area internal to the LGSs, an improvement of a factor of ~4 over the mean tomographic error seen without using predictive techniques (Figure 2). Similar gains are possible for any scenario in which the layer velocity vector is proportional to layer height. Although such an alignment of layer velocities is a rare situation, this example illustrates

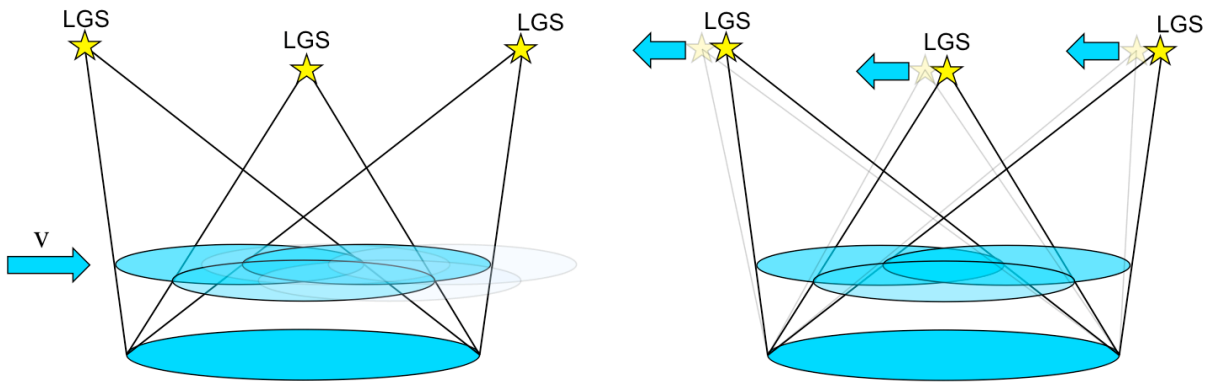

Fig. 1. Schematic of idealized 2-layer frozen flow model. *Left panel:* Frozen flow motion with velocity v on the upper atmospheric layer and a static lower layer. *Right panel:* Same geometry, but with static layers and scanning laser guide stars. With an angular scanning speed of $\omega = v/h$ for the LGSs, where h is the height of the upper layer, the cases in the two panels can be treated equivalently mathematically.

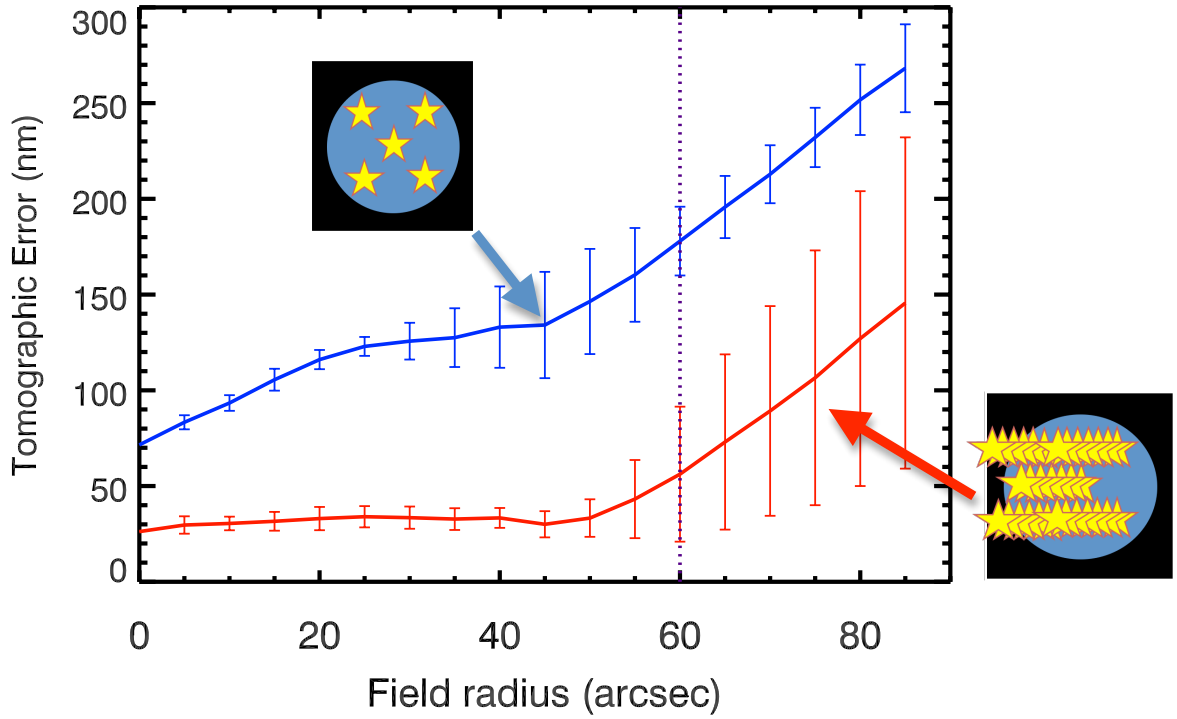

Fig. 2. Geometric tomographic error (RMS nm) as a function of field radius (arcseconds) for the idealized 2-layer frozen flow model described in Section 2. The blue line shows the tomographic error in reconstructing that volume (5 LGSs over 2' diameter) without folding in tomographic reconstructions from previous iterations, i.e., not using a predictive scheme. The red line shows the tomographic error after a single pupil crossing (t = 1.0 s) when using tomographic reconstructions from previous iterations to densely sampled the volume, i.e., using a predictive scheme. Error bars indicate the RMS values over 1000 atmospheric realizations. The dotted violet line shows the radius of the LGS constellation. The inset images show the effective guide star geometry for each case; the multiple "smeared" stars in the predictive case correspond to line-of-sight integrals used from previous time steps. In this simplistic geometry in which the layer velocity is proportional to layer height, significant gains in the tomographic error are realized by using predictive schemes.

that significant gains in the tomographic error are plausible by using predictive schemes that utilize previous tomographic reconstructions.

3. EXPERIMENTAL DESIGN

We now present tomography simulations for a more general case in which wind vectors are not proportional to layer height. This setup uses three laser guide stars on a circle of 2 arcminutes diameter and 3 atmospheric layers with varying C_N^2 profiles (geometry shown in Figure 3). The layer heights in the tomographic analysis are constrained to match those in the true atmospheric model, although the relative strengths are unknown and left to the tomographic code to determine. Atmospheric tip/tilt is assumed to be preserved on the incoming guide star wavefronts. Open-loop operation is assumed. We neither include noise on the wavefront sensors nor the effects of high spatial frequency errors that cannot be sampled by the wavefront sensors. All atmospheric spatial frequencies above Nyquist are removed from simulated phase screens before the tomographic iterations, essentially removing sampling and aliasing errors.

3.1 Tomographic Analysis

For these simulations, we use the TomographySphericalWave (TSW) tool, which performs iterative least-squares back-projection tomography in the Fourier domain.[8] More details about the implementation of this simulator are given in previous publications,[8,15,6] especially Ammons et al. (2012).[16]

The simulations are performed with an 8-meter aperture and 16x16 wavefront sensors for each guide star. Details of wavefront sensing are ignored, and the sensors are assumed to be perfect phase sensors. Twenty tomography iterations are computed for each AO time step with an iteration gain of $a = 0.25$. Three atmospheric cases with different C_N^2 are performed with 200 atmospheric realizations each, with total strength corresponding to $r_{0,500nm} = 16$ cm in each case. In each atmospheric realization, the simulation is performed over 1 simulated second of time at 1 kHz, or at most one pupil crossing time. The wind vectors at each layer are orthogonal and the wind speeds are set to 8 m/s at each layer. The tomographic algorithm converges on a phase volume estimate that agrees with the measured LGS wavefronts to the ~25 RMS nm level at each timestep for all realizations.

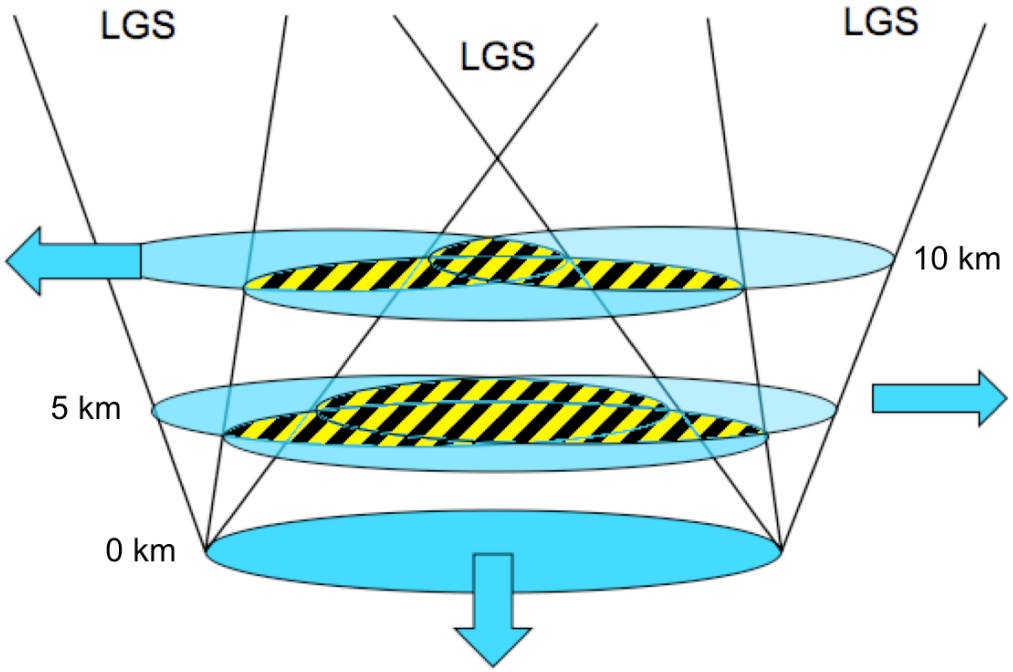

Fig. 3. Three-layer atmospheric geometric with 3 LGSs for predictive simulations described in Section 3. Layers are at 0, 5, and 10 km altitude. Wind directions are perpendicular. Regions of the metapupil sampled by more than one laser guide star are marked with hatched yellow and black diagonal lines.

3.2 Multi-Layer Shift-and-Average Technique

To predict for wind motion, we assume that the wind vector is known for each layer (ignoring the details of wind detection and characterization) and shift-and-average layers taken from a history of tomographic reconstructions generated in previous time steps. Phase voxels at a physical location (**r**,t') (where **r** is a two-dimensional location vector in a given layer of height *h* and *t'* is the current iteration time) are replaced according to

$$\Phi'(\mathbf{r},\ t') = \frac{1}{n' - n_0 + 1} \sum_{n=n_0}^{n'} \Phi(\mathbf{r} - c(n' - n)\mathbf{v}, cn)$$

where n is the zero-indexed timestep number, n' is the current timestep number, c is the time interval between AO iterations (with $t = cn$), and **v** is the known wind velocity vector. The parameter n_0 is the timestep number at which averaging is started.

Only regions of the metapupil that are sampled by more than one LGS are included in the average (hatched regions in Figure 3). Voxels in regions of the metapupil sampled by only one LGS are assumed to be spurious and are not included in the average. The modified volume estimate Φ' is not used to compute tomography for later timesteps, but only used to check the improvement of the phase estimate for each layer.

4. RESULTS AND DISCUSSION

The simulation results are presented in Table 1 and Figures 4 and 5. Table 1 lists the C_N^2 distributions for each of the three cases investigated and the improvement in the phase estimate of each layer at the last time step (t = 1.0 s) with shift-and-averaging relative to the no-prediction case. Case 1 has a median atmosphere (45% of the turbulence above the ground layer), Case 2 is top-heavy (55% above the ground layer) and Case 3 is bottom-heavy (35% above the ground layer). The phase estimates improve for all of the layers for each case by between 3.3% and 12.1%. There is no immediately obvious correlation between the improvement in the phase estimate and the strength of the layer.

Figure 4 shows the average improvement in the layer estimate seen with shift-and-averaging as a function of simulation time for the Case 1 profile. In general, the layer phase estimates improve monotonically with time as more data is accumulated, although the 10 km layer shows evidence of decline in the improvement after t = 0.8 seconds. Figure 5 displays maps of the percent improvement in the layer estimates for the three cases after t = 1.0 second. White values correspond to regions of the metapupil that benefit strongly from shift-and-averaging prediction and darker values correspond to areas where prediction injects error into the estimate. Note that the particular pattern of improvement in the phase estimates is independent of the case and the strength of turbulence in each layer, but appears to be more a function of the LGS geometry.

From Figure 5, it is clear that the majority of the benefit occurs in regions of the metapupil sampled by one LGS that are *downwind* and *at high altitude.* Downwind areas at the edge of the 10 km metapupil see improvements as large as 60%.

Parameter	Case 1	Case 2	Case 3
C_N^2 distribution (%)	[55, 30, 15]	[45, 35, 20]	[65,30,5]
RMS on-axis tomographic error, average (nm)	218	240	145
Average RMS wavefront amplitude (nm)	[802, 436, 328]	[690, 497, 319]	[923, 361, 116]
Improvement in layer estimate with prediction (%)	[7.2, 3.3, 12.1]	[9.2, 3.8, 10.6]	[5.9, 4.8, 11.2]

Table 1. Summary of experimental results and derived parameters. Values for three different layers are grouped in bracketed sets. Results are averaged over 200 realizations.

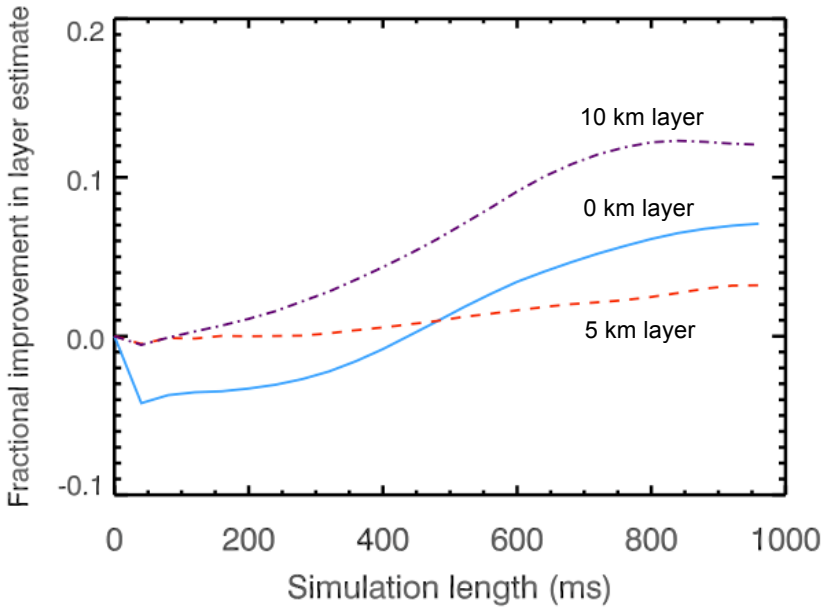

Fig. 4. Trends in the precision of layer phase estimates as a function of simulation time for Case 1. Precision in layer phase estimates is measured in RMS nanometers, comparing to the known depistoned, detilted phase screens at the resolution of the wavefront sensor. All layer estimates improve by between 3 and 13% at the conclusion of the 1 second simulation.

Importantly, the ground layer phase estimate also improves over time in the downwind direction by 10-20%, suggesting that the magnitude of the tomographic errors due to blind modes average down with time and do not introduce systematic errors as they are shifted and averaged.

Figure 6 shows the expected improvement in the geometric tomographic error with field radius, or the error in estimating phase integrals taken through the volume, for an average of the three cases explored here. The radius at which a given tomographic error is reached is expanded by ~20% for this case. This suggests that an MOAO system dominated by geometric tomographic error would see an expansion of 40% of the field of regard over which the correction requirement could be met if prediction were used. These results are similar to those obtained with other multi-layer tomographic testbeds.[17]

These results indicate that even a simplistic predictive control scheme like shift-and-averaging can result in 3-12% improvement in layer phase estimates. *The majority of the benefits occur in sparsely-sampled regions downwind at high altitudes*, where phase altitude cannot be effectively determined by tomography alone. Further work will indicate whether these benefits can be obtained in more realistic atmospheric scenarios. In particular, if the wind vector must be estimated from the telemetry itself, it is expected that errors in those parameters would reduce the efficacy of the prediction. Furthermore, it is also expected that the benefits of shifting-and-averaging would be reduced when applied to real-world turbulence, for which at most 40% of the power of the turbulence is in Taylor frozen flow motion.

5. ACKNOWLEDGEMENTS

Thanks to Michael Hart, Jean-Marc Conan, Anne Costille, and Amélie Parisot for helpful discussions. This work is performed under the auspices of the U.S. Department of Energy by Lawrence Livermore National Laboratory under Contract DE-AC52-07NA27344 with document release number LLNL-PROC-564492.

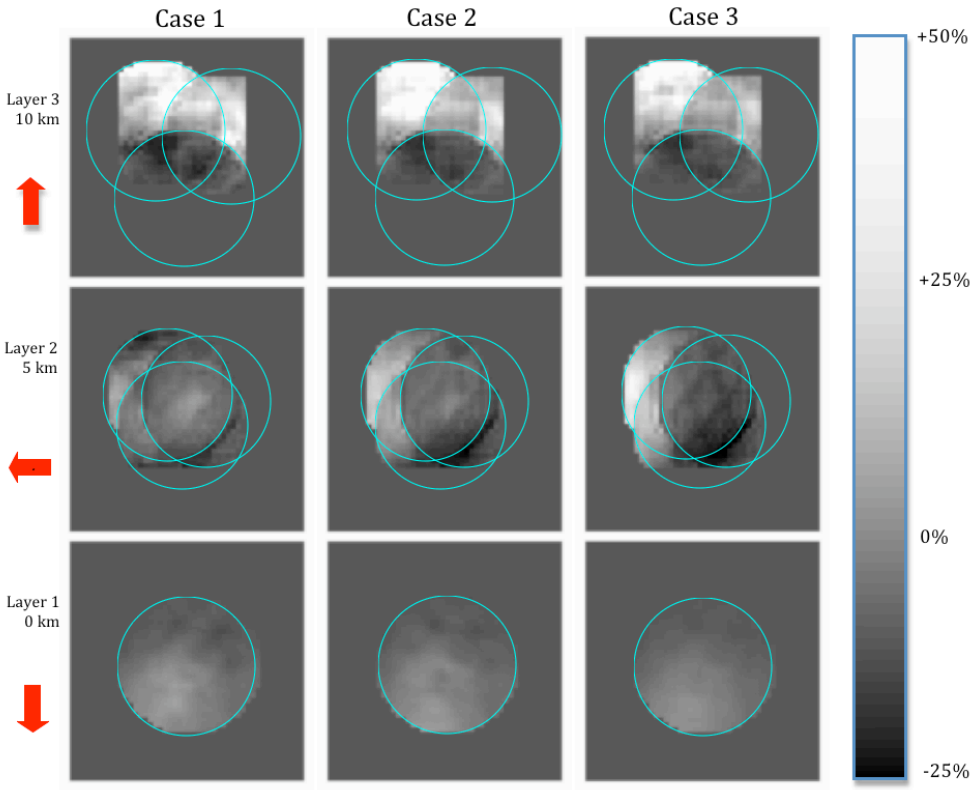

Figure 5. Maps of percent improvement in the RMS deviation between true atmospheric phase and the estimated phase seen with shifting-and-averaging, averaged over 200 realizations. The grayscale range shown in the colorbar is [-25%, +50%], with 0% corresponding to no improvement in the phase estimate with wind prediction at a given subaperture. Each column corresponds to a different atmospheric case; each row corresponds to a different layer for a given case. These measurements are taken at the end of the simulation (t = 1.0 s). The red arrows denote the directions of wind motion for each layer. Aquamarine circles mark the borders of metapupils for each case. In these maps, positive values correspond to regions of the metapupil that benefit from multi-layer predictive control. Note that the majority of the benefits appear downwind in regions sampled by only one or two LGS's in high-altitude layers, although a ~10-20% improvement in seen in the well-sampled ground layer downwind.

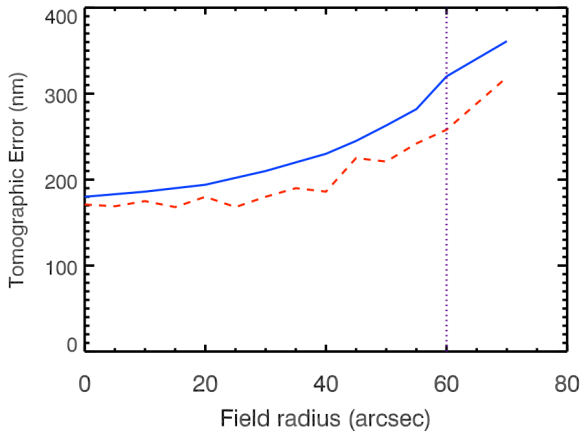

Figure 6. Plot of geometric tomographic error in RMS nanometers as a function of field radius for the Case 1 simulation using shifting-and-averaging predictive control. Tomographic error is assessed at the end of the simulation (1 second), corresponding to approximately one pupil crossing, averaged over 200 atmospheric realizations. The blue solid line shows the tomographic error on wavefronts integrated through the volume without predictive control. The red dashed line shows the calculated tomographic error with predictive control, assuming an improvement in layer estimates as shown in Figure 5.

REFERENCES

[1] Ragazzoni, R., Marchetti, E., and Rigaut, F., "Modal tomography for adaptive optics," Astronomy & Astrophysics 342, 53 (1999).

[2] Viard, E., Hubin, N.N., Le Louarn, M., Delabre, B., Monnet, G.J., and Tokovinin, A.A., "Adaptive optics with four laser guide stars: cone effect correction on large telescopes," proc. SPIE, 4007, 94 (2000).

[3] Fusco, T., Conan, J., Rousset, G., Mugnier, L. M., and Michau, V. "Optimal wave-front reconstruction strategies for multiconjugate adaptive optics," Journal of the Optical Society of America-A, 18, 2527 (2001).

[4] Tokovinin, A., Le Louarn, M., Viard, E., Hubin, N., and Conan, R., "Optimized modal tomography in adaptive optics," Astronomy & Astrophysics, 378, 710 (2001).

[5] Dekany, R.G., Britton, M.C., Gavel, D.T., Ellerbroek, B.L., Herriot, G., Max, C.E., and Véran, J.-P., " Adaptive optics requirements definition for TMT," proc. SPIE, 5490, 879 (2004).

[6] Ammons, S.M., Johnson, L., Laag, E., Kupke, R., Gavel, D.T., Bauman, B.J., and Max, C.E., "Integrated Laboratory Demonstrations of Multi-Object Adaptive Optics on a Simulated 10 Meter Telescope at Visible Wavelengths," Publications of the Astronomical Society of the Pacific, 122, 573 (2010).

[7] Costille, A., Petit, C., Conan, J.-M., Kulcsar, C., Raynaud, H.-F., and Fusco, T., "Wide field adaptive optics laboratory demonstration with closed-loop tomographic control," Journal of the Optical Society of America-A, 27, 469 (2010).

[8] Gavel, D.T., "Tomography for multiconjugate adaptive optics systems using laser guide stars," proc. SPIE, 5490, 1356 (2004).

[9] Poyneer, L.A. & Véran, J.-P., "Toward feasible and effective predictive wavefront control for adaptive optics," proc. SPIE, 7015, 36 (2008).

[10] Johnson, L., Gavel, D.T., Reinig, M., and Wiberg, D., "Wind estimation and prediction for adaptive optics control systems," proc. SPIE, 7015, 92 (2008).

[11] Poyneer, L.A., van Dam, M., & Véran, J.-P., "Experimental verification of the frozen flow atmospheric turbulence assumption with use of astronomical adaptive optics telemetry," Journal of the Optical Society of America-A, 26, 833 (2009).

[12] Johnson, L., Gavel, D.T., and Wiberg, D., "Online wind estimation and prediction for a two-layer frozen flow atmosphere," proc. SPIE, 7736, 92 (2010).

[13] Petit, C., Conan, J.-M., Kulcsár, C., and Raynaud, H-F. "Linear quadratic Gaussian control for adaptive optics and multiconjugate adaptive optics: experimental and numerical analysis," JOSA-A, 26, 1307 (2009).

[14] Parisot, A., Costille, A., Petit, C., and Fusco, T. "Closed-loop tomographic control on HOMER wide-field AO bench: experimental results and identification issues," proc. SPIE, 7736, 107 (2010).

[15] Gavel, D.T., Reinig, M., & Cabrera, C., "Fast hardware implementation of tomography for multi-guidestar adaptive optics," proc. SPIE, 5903, 2 (2005).

[16] Ammons, S.M., Johnson, L., Kupke, R., Gavel, D., Max, C., and Poyneer, L. "Multi-layer predictive control for tomographic wavefront sensing," proceedings of Adaptive Optics for Extremely Large Telescopes 2, held in Victoria, B.C., ed. Véran, J.-P., Fusco, T., and Clénet, Y., in press (2012).

[17] Ammons, S.M., Johnson, L., Laag, E., Kupke, R., and Gavel, D. "Laboratory demonstrations of multi-object adaptive optics in the visible on a 10 meter telescope," proc. SPIE, 7015, 5 (2008).